NUMERICAL INVESTIGATION OF COLLISION-INDUCED BREAKUP OF RAINDROPS. PART I: METHODOLOGY AS WELL AS DEPENDENCIES ON COLLISION ENERGY AND EXCENTRICITY

J. Schlottke[1] **, W. Straub**[2] **, K. D. Beheng**[2] **and B. Weigand**[1]

[1] Institut für Thermodynamik der Luft- und Raumfahrt (ITLR), Universität Stuttgart, Pfaffenwaldring 31, 70569 Stuttgart, Germany, e-mail: jan.schlottke@itlr.uni-stuttgart.de

[2] Institut für Metereologie und Klimaforschung, Universität Karlsruhe/Forschungszentrum Karlsruhe, Hermann-von-Helmholz-Platz 1, 76344 Eggenstein-Leopoldshafen, Germany, e-mail: winfried.straub@imk.fzk.de

Numerical investigations of binary raindrop collisions, comprising the drop pairs of Low and List (1982a), have been performed using a DNS tool based on the Volume-of-Fluid method. Looking at the coalescence efficiencies as well as the number and sizes of the fragment droplets, both agreement and discrepancies between the numerical simulations and the experimental data of Low and List (1982a) are observed. The results show that the size distribution of fragments is dependent on the collision energy and is shifted to smaller fragments for higher energies. In the second part of this paper, Straub et al. (2008) present new parameterizations of coalescence efficiencies and fragment size distributions based on the results obtained.

1 INTRODUCTION

Collision-induced breakup resulting from binary collisions of large raindrops is considered to be the principal mechanism limiting the size of raindrops (Pruppacher and Klett 1997). During this process, two raindrops that are moving at different velocities temporarily coalesce into one larger drop. The final outcome can be a single large raindrop or remnants of the original raindrops with a number of secondary droplets of different sizes. Comprehensive experimental investigations habe been presented in the past by Low and List (1982a) who, however, concentrated on very few drop pairs. Consequently the data base from which parameterizations have been derived is rather small and incomplete. Furthermore, the parameters relevant to this process like droplet velocity, droplet size, and most notably collision excentricity could not be determined with high accuracy. To overcome these deficiencies Beheng et al. (2006) have performed numerical experiments by computational simulations of binary collisions for same drop pairs as Low and List (1982a) and for some more drop pairs. The present study is a further extension of the work of Beheng et al. (2006) by again increasing the range of drop pair combinations and by additionally investigating the influence of excentricity and impact energy. To this end, the DNS-CFD code FS3D (Free Surface 3D) which has been developed at ITLR is applied. It solves the incompressible Navier-Stokes equations and employs the Volume of Fluid (VOF) method to account for multiple phases. The free surface is reconstructed using the PLIC method and the convective transport is based on this reconstruction.

2 FORMULATION AND NUMERICAL METHOD

The applied code FS3D has been used for numerous investigations of drop dynamics in the past and is well validated. Gotaas et al. (2007) for example studied the effect of viscosity on binary droplet collisions, Rieber and Frohn (1999) simulated the process of drops splashing onto a liquid film.

2.1 Governing Equations

The representation of different phases is based on the Volume of Fluid (VOF) method by Hirt and Nichols (1981). In order to distinguish between the liquid and the gaseous phase, the additional field variable f is introduced. f is defined as

$$f(\mathbf{x},t) = \begin{cases} 0 & \text{in the gaseous phase} \\ 0 < f < 1 & \text{in cells containing a part of the interface} \\ 1 & \text{in the liquid phase} \end{cases} \tag{1}$$

and is transported by

$$\frac{\partial f}{\partial t} + \nabla \cdot (f\mathbf{u}) = 0. \tag{2}$$

In order to maintain a sharp interface, the convective transport of f is performed based on the

reconstructed interface using the Piecewise Linear Interface Calculation (PLIC) method by Rider and Kothe (1998), thus minimizing numerical diffusion.

The governing balance equations for momentum read

$$\frac{\partial(\rho\mathbf{u})}{\partial t} + \nabla\cdot(\rho\mathbf{u})\otimes\mathbf{u} = -\nabla p + \rho\mathbf{k} + \nabla\cdot\left[\mu\left(\nabla\mathbf{u} + (\nabla\mathbf{u})^T\right)\right] + \mathbf{f}_\gamma \quad (3)$$

where $\mathbf{k}$ represents an external body force (e.g. gravity). The surface tension is included by the volume force $\mathbf{f}_\gamma$.

The continuity equation for the considered incompressible flow is given by

$$\nabla\cdot\mathbf{u} = 0. \quad (4)$$

The local fluid properties are obtained by applying the *one-field* formulation. Viscosity and density are hence calculated by

$$\mu(\mathbf{x},t) = \mu_l f(\mathbf{x},t) + (1-f(\mathbf{x},t))\mu_g, \quad (5)$$
$$\rho(\mathbf{x},t) = \rho_l f(\mathbf{x},t) + (1-f(\mathbf{x},t))\rho_g. \quad (6)$$

2.2 Spatial and Temporal Discretization

The spatial discretization of the equations is done using the Finite Volume method on a staggered grid and is of second order accuracy. The temporal integration is performed using the Crank-Nicholson method. A fast and robust multigrid solver is used for the projection of the velocity field onto one fulfilling eq. (4).

3 NUMERICAL SETUP AND SIMULATION PROCEDURE

All presented simulations were performed using a 3D computational domain with free-slip condition on the lateral walls and periodic boundary conditions on the bottom and top walls. This setup permits a numerically justifiable effort for the large number of conducted simulations as the collision process can be observed for a rather long time period using a limited computational grid. The spatial resolution was chosen to be 100 µm for all cases except investigations on grid dependency where a spatial resolution of 50 µm has been applied. According to the drops' sizes, different grids were employed, resulting in approx. 16×10^6 cells for the largest one (2.56^3 cm^3) used for standard calculations and nearly 135×10^6 cells for grid dependency investigations.

For the initial placement and velocities v of the drops, terminal fall velocities have been calculated following Beard (1976). The vertical distance between the drops was set to $\Delta y = v\Delta t$ with Δt=0.5ms, allowing for an interaction of the drops with their surrounding flow field to some extent. The nonspherical shape of large drops was considered by initializing them as ellipsoids with the ratio of the equatorial radii to the polar radius according to Beard and Chuang (1987). The excentricity of the droplet collisions, defined as the ratio of the distance of the drops' centers δ to the arithmetic mean of their diameters d (with subscripts L and S for the large and the small drop, respectively)

$$\epsilon = \frac{2\delta}{d_L + d_S} \quad (7)$$

has been varied from 0.05 to 0.95 with six different excentricities (ϵ=0.05, 0.2, 0.4, 0.6, 0.8, 0.95). The initial setup is sketched on a plane through the drops' centers in figure 1. Material properties for water and air were chosen at 20° C with a surface tension of σ=73×10^{-3} N/m.

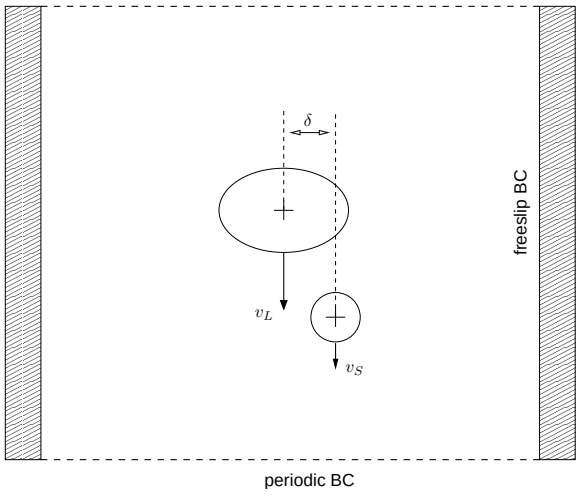

Figure 1: Numerical setup

The simulations were performed until a stable outcome of the collision process was reached. This condition was assumed to be fulfilled by a visual assessment of the results especially with the number of fragments becoming stationary. The number and size of the fragments were then determined by the use of a region growing approach. Mass conservation was satisfied for all cases. In order to compare to data from literature, the obtained results for different excentricities have been weighted according to their probability.

4 RESULTS

Overall, 32 drop pairs were investigated. Details of the drop diameters, the collision and surface energy and the resulting Weber number are given in table 1, an overview of the drop pairs considered is shown by figure 2. The 10 drop pairs investigated by Low and List (1982a) are included and listed as numbers 1-10 in table 1, those additionally simulated by Beheng et al. (2006) as 11-18; the remaining drop pairs (19-32) are considered to cover the pairs' matrix as complete as

No.	d_L	d_S	CKE	S_c	We	No.	d_L	d_S	CKE	S_c	We
1	0.18	0.04	0.33	0.75	0.44	17	0.32	0.04	0.73	2.35	0.31
2	0.4	0.04	0.86	3.67	0.23	18	0.41	0.14	9.6	3.96	2.43
3	0.44	0.04	0.9	4.44	0.2	19	0.24	0.06	1.29	1.33	0.97
4	0.18	0.07	0.92	0.77	1.19	20	0.3	0.07	2.43	2.08	1.17
5	0.18	0.1	0.99	0.83	1.2	21	0.36	0.07	2.97	2.99	0.99
6	0.3	0.1	4.18	2.11	1.98	22	0.45	0.07	3.43	4.66	0.74
7	0.36	0.1	5.46	3.01	1.81	23	0.12	0.1	0.07	0.45	0.15
8	0.46	0.1	6.62	4.89	1.35	24	0.41	0.1	6.18	3.89	1.59
9	0.36	0.18	8.55	3.21	2.66	25	0.25	0.12	3.14	1.54	2.04
10	0.46	0.18	12.53	5.04	2.48	26	0.3	0.12	5.04	2.15	2.34
11	0.06	0.04	0.01	0.09	0.12	27	0.36	0.12	6.93	3.05	2.28
12	0.12	0.04	0.12	0.34	0.35	28	0.46	0.12	8.7	4.91	1.77
13	0.12	0.06	0.24	0.36	0.68	29	0.36	0.14	8.07	3.09	2.61
14	0.25	0.04	0.55	1.44	0.38	30	0.18	0.16	0.13	1.06	0.12
15	0.24	0.09	2.36	1.37	1.73	31	0.41	0.16	10.62	4.01	2.65
16	0.27	0.15	3.93	1.86	2.11	32	0.25	0.18	1.88	1.77	1.06

Table 1: Investigated drop pairs, d_L and d_S in [cm], CKE and S_c in [µJ]

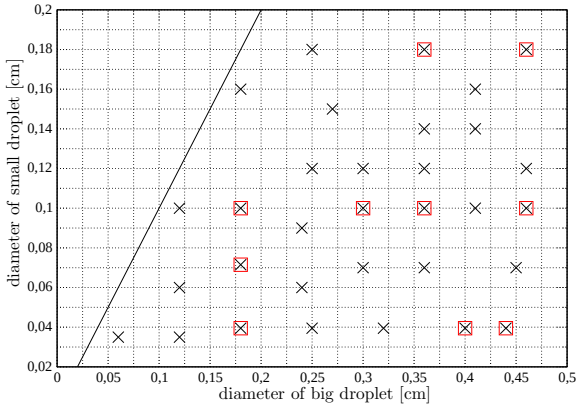

Figure 2: Investigated drop pairs; red squares indicate the pairs studied by Low and List (1982a).

possible.

The collision energy of the drop pairs CKE is calculated by (ρ_l = bulk density of water)

$$CKE = \frac{\pi}{12}\rho_l \frac{d_L^3 d_S^3}{d_L^3 + d_S^3}\left(v_L - v_S\right)^2, \qquad (8)$$

the surface energy S_c of the coalesced system is given by

$$S_c = \pi\sigma\left(d_L^3 + d_S^3\right)^{2/3}. \qquad (9)$$

The Weber number We is the ratio of the aforementioned energies

$$We = \frac{CKE}{S_c}. \qquad (10)$$

4.1 Collision Outcomes

Results are shown exemplarily in figures 3 and 4 for two different drop pairs with 5 collision excentricities, respectively. The two pairs of drops chosen for this comparison have high (Pair 10, CKE=12.53 µJ) and low (Pair 16, CKE=3.93 µJ) collision energies.

For Pair 10 shown in figure 3 the dependency of the breakup mode on excentricity is evident. As it can be expected for the considered collision energy, there is disc breakup for ϵ=0.05 and ϵ=0.2, resulting in numerous small droplets of different sizes after the collision process. For ϵ=0.4 and ϵ=0.6, the breakup mode is sheet breakup and the size distribution of the secondary droplets is more homogeneous. For ϵ=0.8 and ϵ=0.95 (not shown), finally, there is filament breakup, the initial drops persist after the collision process with almost no change in drop size. Moreover some additional, very small droplets are produced. An overview on the mentioned dependency is also shown in figure 9 for the discussed droplet pair and two supplemental pairs with lower collision energies.

The collision outcomes for Pair 16 are shown in figure 4. For ϵ=0.05 and ϵ=0.2 the two drops form a single larger permanent drop after collison. For the other excentricities, there is filament breakup with no additional droplets for ϵ=0.4 and ϵ=0.8; some small secondary droplets are produced for ϵ=0.6.

4.2 Budget of Energy

To get a picture of the evolution of energies during a collision process, the temporal development

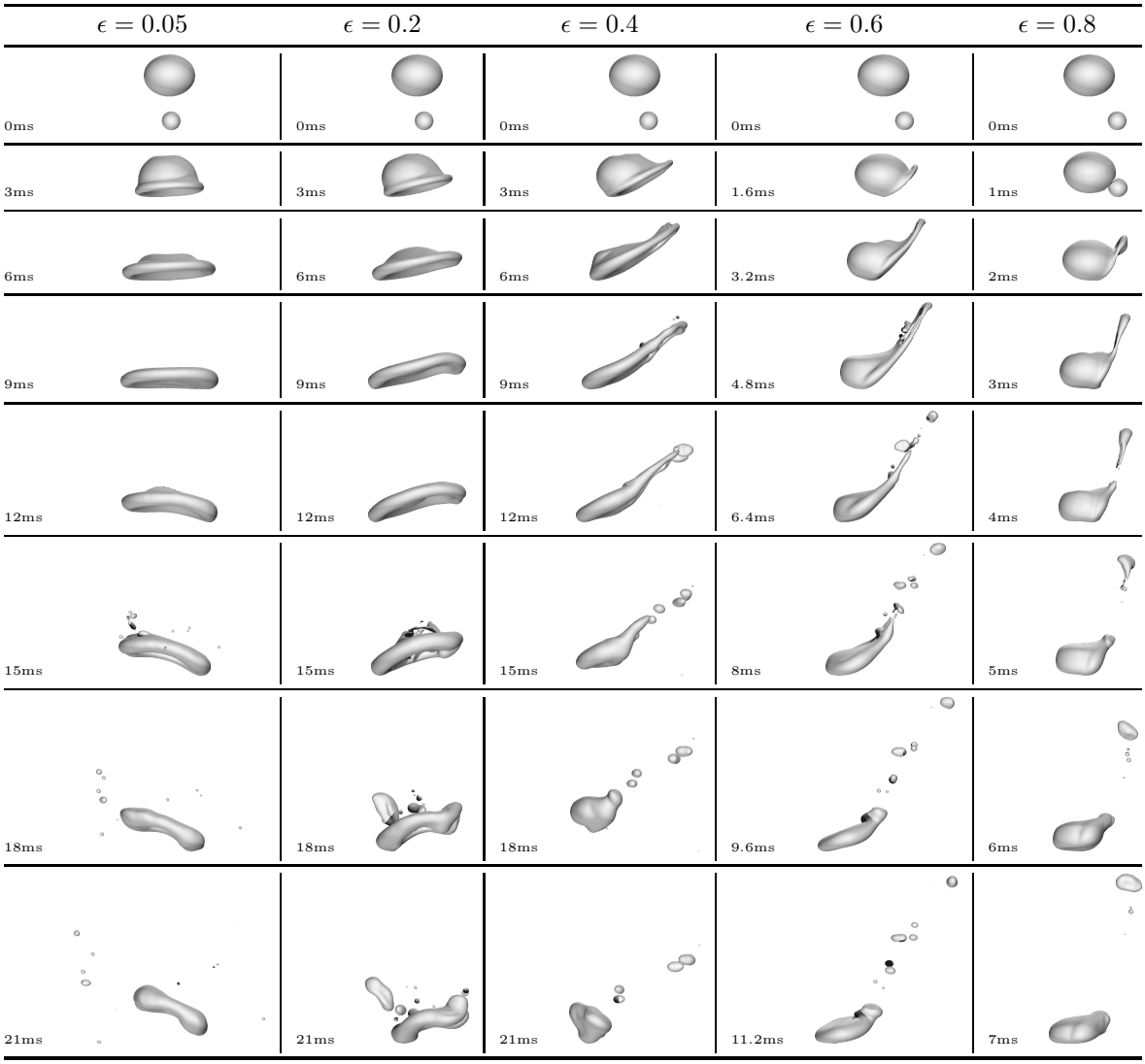

Figure 3: Snapshots of droplet collisions at different times, Pair 10 (CKE=12.53µJ)

of the kinetic energy of the fluid contained in the system, the surface energy and the surface area is depicted for Pair 26, ϵ=0.6, in figure 5. Gravity was set to zero for this consideration. The appropriate images of the collision process are presented in figure 6. The surface energy is obtained as the product of surface area and surface tension. For convenience, both the initial surface energy and the initial kinetic energy are plotted starting from zero.

Looking at the surface area and energy, there is a sudden drop as the drops coalesce. This area reduction is caused by the contact of the two drops and the merging of their surfaces. Subsequently, the relative velocity leads to a strong deformation of the generated larger drop whereas the surface area is increased by about 50 %. That is followed by the separation into one large drop and several smaller droplets where the drops attain a roughly spherical shape and oscillate.

The kinetic energy decreases at first during the aggregation phase of the drops. Then it increases again and reaches a momentary maximum as the liquid disintegrates and surface energy gets transformed. Subsequently, the kinetic energy is continuously reduced, presumably caused by viscous dissipation due to the inner flowfield of the drops and interaction with the surrounding gas.

4.3 Coalescence Efficiency

The coalescence efficiency E_c is defined as the propability of coalescence for a binary collision process with a single drop resulting. For an experimental study consisting of numerous repetitions for one drop pair, E_c is obtained by dividing the number of collisions leading to coalescence c_c by

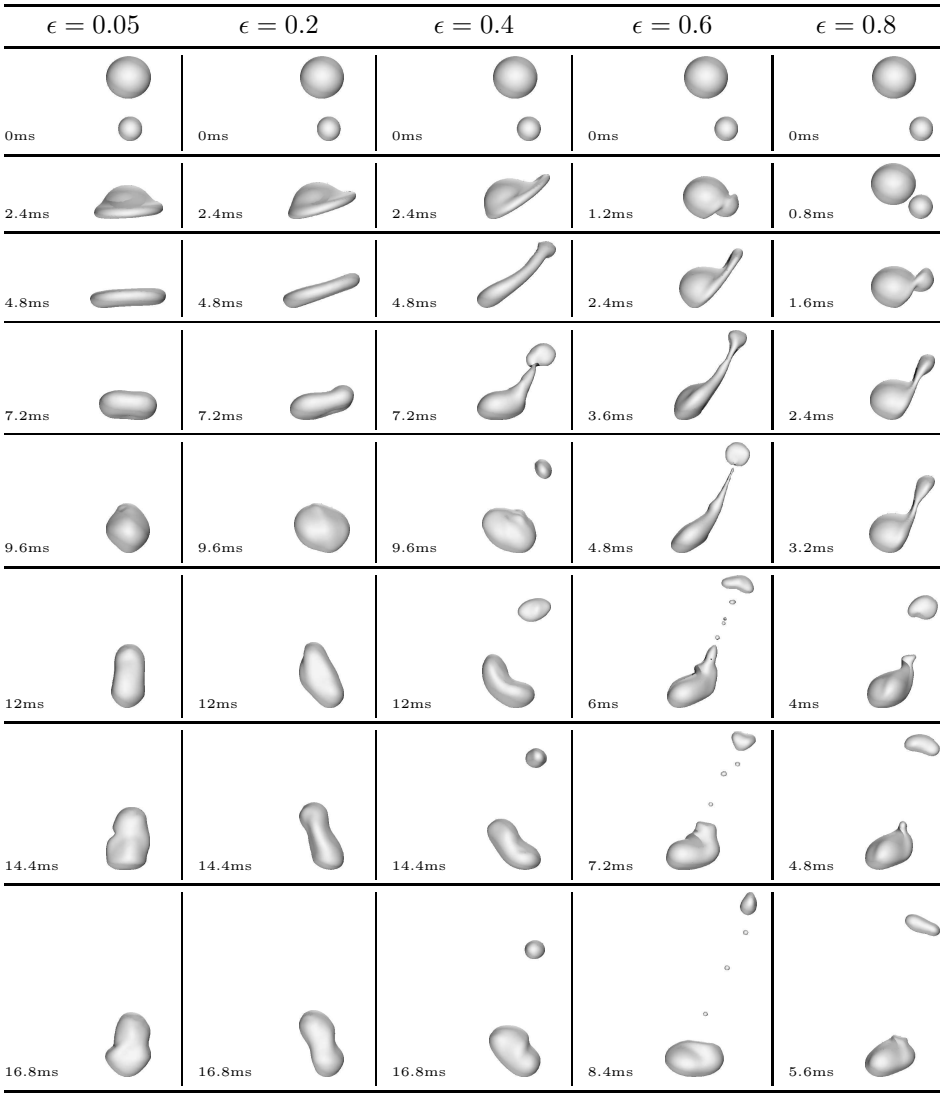

Figure 4: same as figure 3 but for Pair 16 (CKE=3.93µJ)

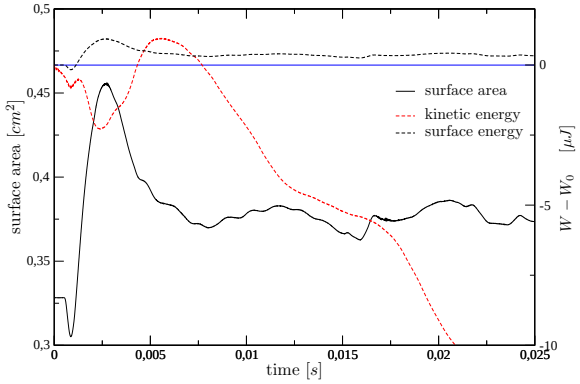

Figure 5: Temporal evolution of kinetic energy, surface energy and surface area for drop pair 26, ϵ=0.6; left ordinate: surface area, right ordinate: energies

the total number of collisions c:

$$E_c = c_c/c. \tag{11}$$

It should be mentioned that an equipartition of collisions over the collision cross section (collision excentricities) is assumed for this approach. Keeping in mind the strong dependency of collision outcomes on excentricity, experimental results for E_c seem to be quite sensitive to systematic errors influencing the aforementioned equipartition.

On the other hand, collisions with six different excentricities per drop pair were investigated numerically for the present study. Here, each collision is representing all collisions taking place in the according annulus of the projected collision cross section (circle with radius $r_L + r_S$). The result for one excentricity ϵ_i is weighted with the area of the corresponding annulus (δ_i = separa-

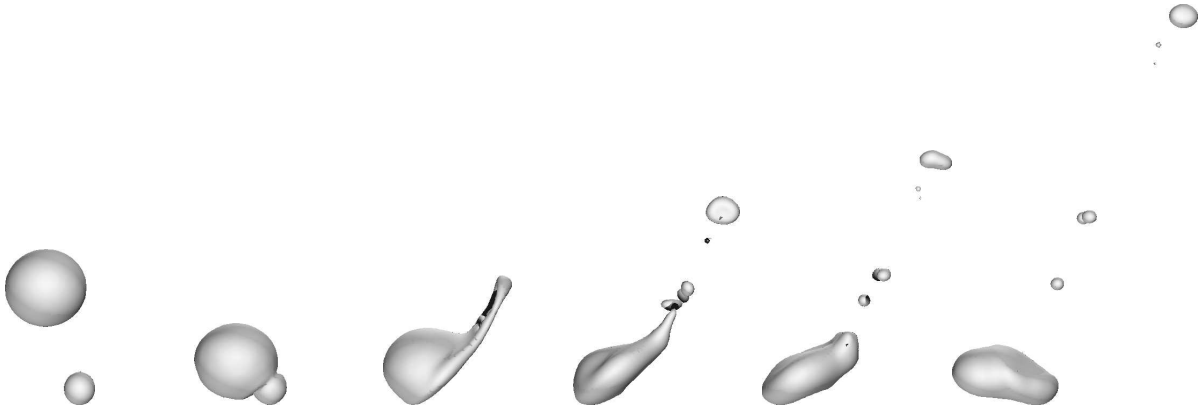

Figure 6: Collision process of Pair 26, ϵ=0.6

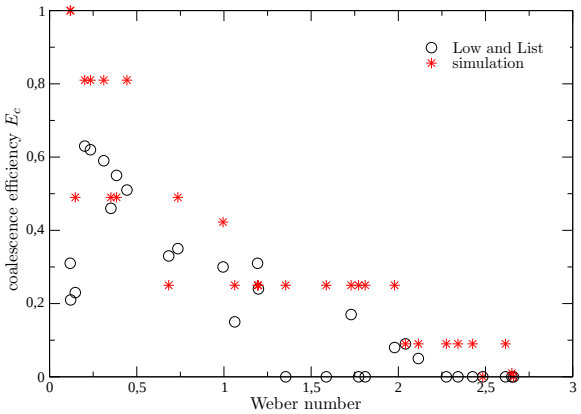

Figure 7: Coalescence efficiency vs. Weber number for all drop pairs. Numerically obtained results (stars) and values from the parameterization by Low and List (1982b) (circles)

tion distance, cf. figure 1)

$$A_{\circledcirc,i} = 2\pi\delta_i\Delta\delta_i = 2\pi\left(r_L + r_S\right)^2\epsilon_i\Delta\epsilon_i. \qquad (12)$$

Hence the coalescence efficiency is calculated by

$$\begin{aligned} E_c &= \sum_{ic} A_{\circledcirc,ic} / \sum_i A_{\circledcirc,i} \\ &= \sum_{ic} \epsilon_{ic}\Delta\epsilon_{ic} / \sum_i \epsilon_i\Delta\epsilon_i \end{aligned} \qquad (13)$$

where ic identifies excentricities for which coalescence occurs.

The results for the investigated drop pairs are plotted in figure 7 as function of the Weber number. Values obtained by the parameterization of Low and List (1982b) are shown additionally. Here, the agreement is quite good. Looking at the experimental values, there are several outliers with E_c=0 that do not seem physical; they are not reproduced by the numerical results. For small Weber numbers, the deviation between numerical and experimental values is increasing. Whereas the coalescence efficiency of the simulations is approaching 1, the efficiency given by the Low and List parameterization is dropping to values of approximately 0.3. This behaviour can be explained by the illegitimate application of the parameterization to the region of very low collision energies which has not been investigated by Low and List. For the numerical results on the other hand, the bouncing process taking place for very low relative velocities can not be simulated due to the employed numerical method, thus leading to values of E_c which are too large.

4.4 Number of Fragments and Fragment Size Distribution

The mean number of fragments $\overline{n}$ is calculated analogously to the coalescence efficiency E_c:

$$\overline{n} = \sum_i n_i\epsilon_i\Delta\epsilon_i / \sum_i \epsilon_i\Delta\epsilon_i. \qquad (14)$$

The spectral number $\overline{p_j}(D_j)$, representing the number of fragments in the diameter interval $D_j \pm \Delta D_j/2$, is given by

$$\overline{p_j} = \frac{\sum_i n_{j,i}\epsilon_i\Delta\epsilon_i / \sum_i \epsilon_i\Delta\epsilon_i}{\Delta D_j} \qquad (15)$$

where $n_{j,i}$ is the number of fragments for excentricity i encountered in the according diameter interval.

The mean number of fragments obtained for all investigated drop pairs is depicted in figure 8 together with values calculated by the Low and List parameterization. The development is very similar for both cases. However, the numerically obtained values are slightly smaller than those from the experiments, mainly for high collision energies. This is, amongst other reasons, due to an insufficient spatial resolution of the computational domain. As shown below in section 4.6, the numerical results are not grid independent with respect to the generation of very small fragment

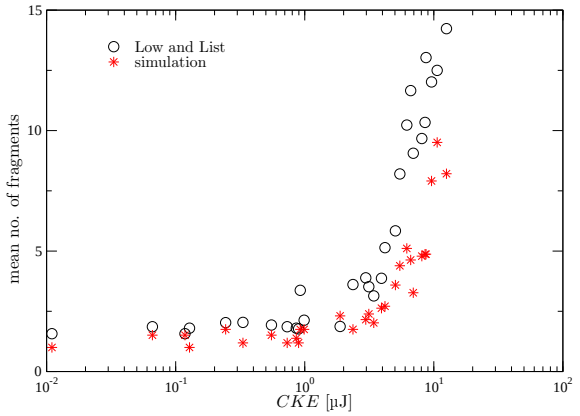

Figure 8: Mean number of fragments vs. collision energy found from the numerical simulations (stars) and from the experiments of Low and List (1982a)

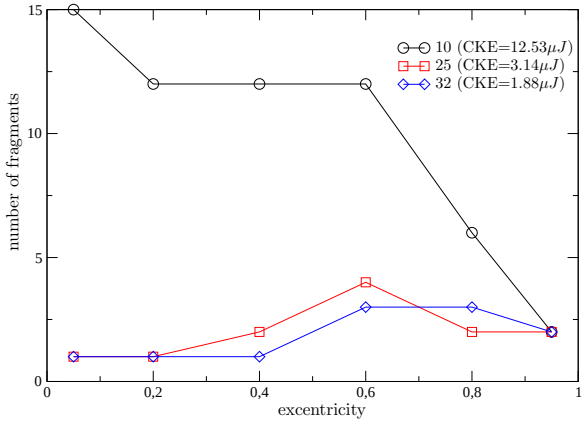

Figure 9: Fragment number vs. excentricity for pairs of different CKE as indicated

droplets which appear numerously for high collision energies.

Fragment size distributions in spectral resolution are shown for all investigated drop pairs in appendix A. The comparison to the Low and List parameterization shows both agreement as well as discrepancies. Whereas the agreement between numerical and experimental results is good for emerging larger fragments, large deviations can be observed especially for very small fragments. This finding can be explained by the already mentioned grid dependency. On the other hand, the experimental results may have been influenced by systematic errors which is particularly important if one takes into account the strong dependency on excentricity as it is shown in the following section.

4.5 Influence of Excentricity

The number of fragments versus excentricity is plotted exemplarily in figure 9 for 3 pairs with different CKE.
As already stated, there is a strong influence of the collision parameter excentricity on the collision outcome. However, this statement is not unambiguous. Looking at high collision energies, a disc mode breakup occurs for low excentricities and multiple small fragments are produced. Increasing excentricity leads to a decreasing number of secondary droplets until the initial drops persist for a grazing collision.
On the other hand, the behaviour in case of medium and low collision energies is contrary. While the two drops coalesce for almost central collisions and persist for grazing collisions, a number of fragment droplets is produced in between.

4.6 Assessment of Results

Assessing the obtained numerical results, various factors have to be considered. The most relevant ones seem to be both the spatial resolution and the boundary conditions.

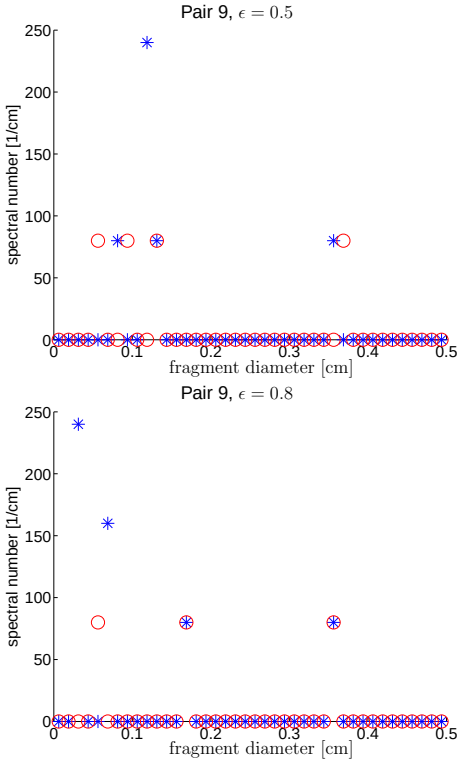

Figure 10: Influence of spatial resolution for pair 9, $\epsilon = 0.5$ and $\epsilon = 0.8$. $\Delta x = 100$µm (red circles) and $\Delta x = 50$µm (blue stars).

In order to elucidate the grid dependency of the results, particular cases have been simulated with doubled spatial resolution, resulting in $\approx 135\times 10^6$ control volumes. The results for the standard resolution (Δx=100µm) and the fine resolu-

tion (Δx=50µm) are shown in figure 10 for Pair 9, ϵ=0.5 and ϵ=0.8. It is well known that the ability of the Volume of Fluid method which is employed for tracking the interface to correctly reproduce the physical behaviour of small ligaments is quite sensitive to the spatial resolution of the grid. This fact is reflected by the presented results. For both excentricities, there is a higher number of small fragments in case of finer grid resolution. For larger fragments, however, it is important to point out that there is only a minor discrepancy of results applying either a fine or a coarse grid. From a physical point of view it seems feasible to apply a lower radius limit of fragment droplets to be considered as very small droplets may evaporate quickly and thus do not contribute to the coalescence-collision process.

As for the boundary conditions, the drawback of the presented approach with periodic boundary conditions is that the drops are falling in their own wake which is of major importance to large droplets where the aerodynamic influence of the oncoming flow plays an important role for the deformation and the breakup process. Future investigations will therefore be performed with a moving frame of reference, thus facilitating a natural flow approaching the drops.

5 CONCLUSION, PERSPECTIVE

The collision process of different pairs of raindrops has been investigated numerically. The drop pairs studied by Low and List (1982a) are amongst the considered pairs. Comparing to their experimental results, there are both agreement as well as discrepancies.

Future investigations will focus on the use of a moving frame of reference with a specific inflow boundary condition. Thus, more realistic simulations are expected. Clearly the according simulations will significantly increase the numerical efforts.

The results presented in this paper are used by Straub et al. (2008) to create a new parameterization of coalescence efficiencies and fragment size distributions.

ACKNOWLEDGEMENT

The simulations were performed on the national super computer NEC SX-8 at the High Performance Computing Center Stuttgart (HLRS) under the grant number FS3D/11142. The authors also gratefully acknowledge support by the German Research Foundation (DFG) under grants BE 2081/7-1 and WE 2549/17-1 in the framework of the priority program Quantitative Precipitation Prediction.

NOMENCLATURE

CKE	collision energy	J
c_c	no. of coll. leading to coalescence	-
c	total number of collisions	-
d	(volume equivalent) diameter	m
D	fragment diameter	m
E_c	coalescence efficiency	-
f	VOF variable	-
$\mathbf{f}_\gamma$	surface tension term	N/m^3
$\mathbf{k}$	body force (gravity)	m/s^2
m	mass	kg
n	number of fragments	-
$\overline{n}$	mean number of fragments	-
p	pressure	Pa
$\overline{p_j}$	spectral number	1/m
r	radius	m
S_c	surface energy	J
t	time	s
$\mathbf{u}$	velocity	m/s
v	vertical velocity	m/s
W	energy	J
$\mathbf{x}$	position	m
Δx	grid resolution	m

Greek

δ	distance	m
ϵ	excentricity	-
μ	viscosity	kgm/s
ρ	density	kg/m^3
σ	surface tension	N/m

Dimensionless quantities

We	Weber number	$(= CKE/S_c)$

Subscripts

0	initial
g	gas
i, j	indices
l	liquid
L	large droplet
S	small droplet

REFERENCES

K. V. Beard. Terminal velocity and shape of cloud and precipitation drops aloft. *J. Atmos. Sci.*, 33:851–864, 1976.

K. V. Beard and C. Chuang. A new model for the equilibrium shape of raindrops. *J. Atmos. Sci.*, 44:1509–1511, 1987.

K. D. Beheng, K. Jellinghaus, W. Sander, N. Roth, and B. Weigand. Investigation of collision-induced breakup of raindrops by numerical simulations: First results. *Geophys. Res. Lett.*, 33, 2006.

C. Gotaas, P. Havelka, H. Jakobsen, H. Svendsen, M. Hase, N. Roth, and B. Weigand. Effect of viscosity on droplet-droplet collision outcome: Experimental study and numerical comparison. *Phys. Fluids*, 19, 2007.

C.W. Hirt and B.D. Nichols. Volume of fluid (VOF) method for the dynamics of free boundaries. *J. Comput. Phys.*, 39:201–225, 1981.

T. B. Low and R. List. Collision, coalescence and breakup of raindrops: Part i: Experimentally established coalescence efficiencies and fragment size distribution in breakup. *J. Atmos. Sci.*, 39:1591–1606, 1982a.

T. B. Low and R. List. Collision, coalescence and breakup of raindrops: Part ii: Parameterization of fragment size distributions. *J. Atmos. Sci.*, 39:1607–1618, 1982b.

H. R. Pruppacher and J. D. Klett. *Microphysics of Clouds and Precipitation*. Springer, New York, 1997.

W.J. Rider and D.B. Kothe. Reconstructing volume tracking. *J. Comput. Phys.*, 141:112–152, 1998.

M. Rieber and A. Frohn. A numerical study on the mechanism of splashing. *Int. J. Heat Fluid Flow*, 20:455–461, 1999.

W. Straub, J. Schlottke, K. D. Beheng, and B. Weigand. Numerical investigation of collision-induced breakup of raindrops. part ii: Parameterizations of coalescence efficiencies and fragment size distributions. In *ICCP*, 2008.

A Spectral numbers

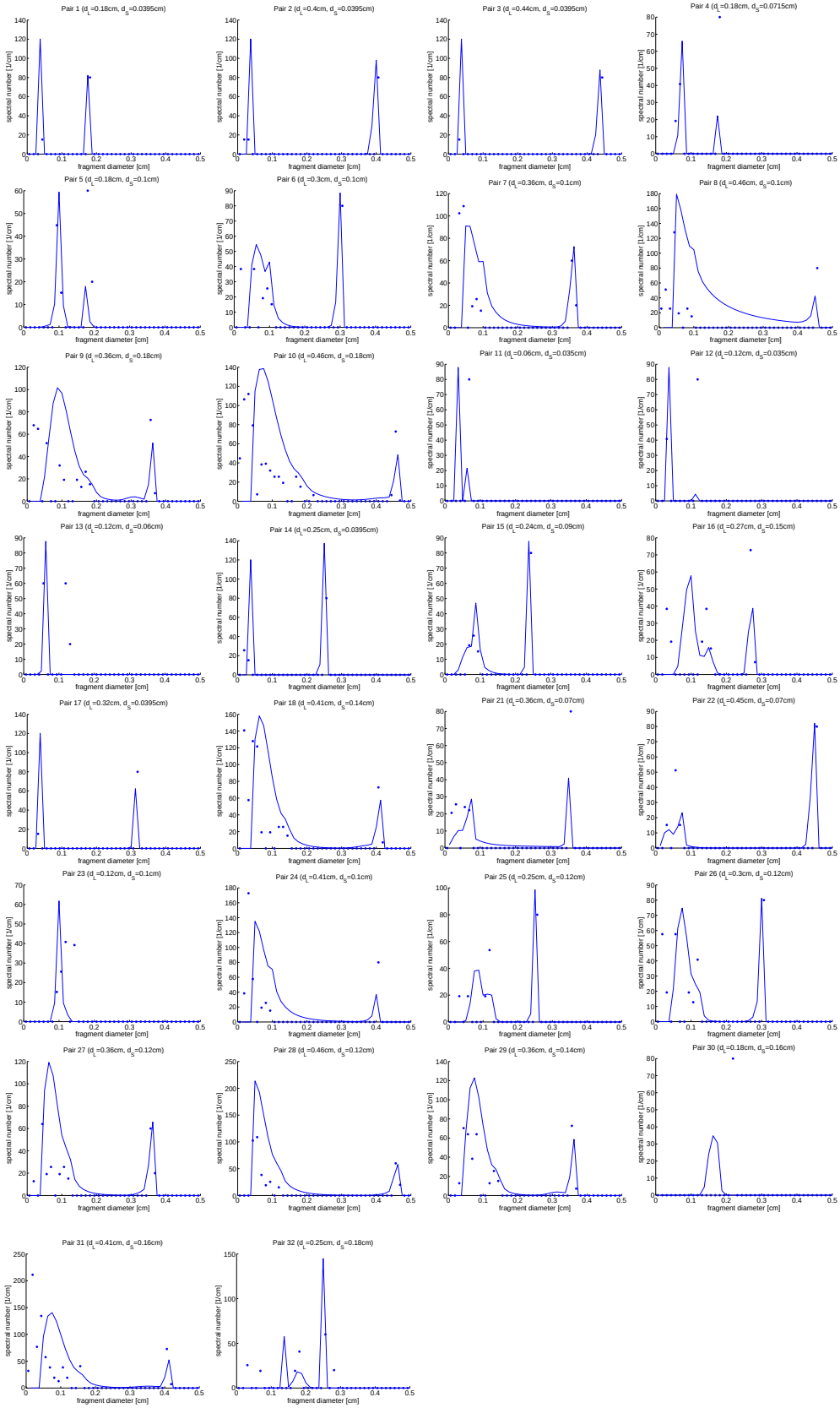

Figure 11: Spectral numbers of fragments as function of fragment diameter for d_L and d_S as indicated. Stars denote present results, lines those according to the parameterization of Low and List (1982b).